

Impact of remineralization profile shape on the air-sea carbon balance

Jonathan Maitland Lauderdale¹ and B. B. Cael²

¹Department of Earth, Atmospheric and Planetary Sciences, Massachusetts Institute of Technology, Cambridge, MA 02139, USA.

²Ocean Biogeochemistry and Ecosystems, National Oceanography Centre, Southampton, SO14 3ZH, UK.

Key Points:

- Six alternative flux profiles fit to a Martin curve yield large differences in atmospheric carbon.
- Structural uncertainty comprises one third of total uncertainty in the ocean's biological pump.

Plain Language Summary

The ocean's "biological pump" regulates atmospheric carbon dioxide levels and climate by transferring organic carbon produced at the surface by phytoplankton to the ocean interior via "marine snow", where the organic carbon is consumed and respired by microbes. This surface to deep transport is usually described by a power-law relationship of sinking particle concentration with depth. Uncertainty in biological pump strength can be related to different variable values ("parametric" uncertainty) or the underlying equations ("structural" uncertainty) that describe organic matter export. We evaluate structural uncertainty using an ocean biogeochemistry model by systematically substituting six alternative remineralization profiles fit to a reference power-law curve. Structural uncertainty makes a substantial contribution, about one third in atmospheric $p\text{CO}_2$ terms, to total uncertainty of the biological pump, highlighting the importance of improving biological pump characterization from observations and its mechanistic inclusion in climate models.

Corresponding author: JML, jml1@mit.edu

Corresponding author: BBC, cael@noc.ac.uk

Abstract

The ocean’s “biological pump” significantly modulates atmospheric carbon dioxide levels. However, the complexity and variability of processes involved introduces uncertainty in interpretation of transient observations and future climate projections. Much work has focused on “parametric uncertainty”, particularly determining the exponent(s) of a power-law relationship of sinking particle flux with depth. Varying this relationship’s functional form introduces additional “structural uncertainty”. We use an ocean biogeochemistry model substituting six alternative remineralization profiles fit to a reference power-law curve, to systematically characterize structural uncertainty, which, in atmospheric pCO₂ terms, is roughly 50% of parametric uncertainty associated with varying the power-law exponent within its plausible global range, and similar to uncertainty associated with regional variation in power-law exponents. The substantial contribution of structural uncertainty to total uncertainty highlights the need to improve characterization of biological pump processes, and compare the performance of different profiles within Earth System Models to obtain better constrained climate projections.

1 Introduction

Carbon and nutrients are consumed by phytoplankton in the surface ocean during primary production, leading to a downward flux of organic matter. This “marine snow” is transformed, respired, and degraded by heterotrophic organisms in deeper waters, ultimately releasing those constituents back into dissolved inorganic form. Oceanic overturning and turbulent mixing returns resource-rich deep waters back to the sunlit surface layer, sustaining global ocean productivity. The “biological pump” maintains this vertical gradient in nutrients through uptake, vertical transport, and remineralization of organic matter, storing carbon in the deep ocean that is isolated from the atmosphere on centennial and millennial timescales, lowering atmospheric CO₂ levels by hundreds of microatmospheres (Volk & Hoffert, 1985; Ito & Follows, 2005). The biological pump resists simple mechanistic characterization due to the complex suite of biological, chemical, and physical processes involved (Boyd et al., 2019), so the fate of exported organic carbon is typically described using a depth-dependent profile to evaluate the degradation of sinking particulate matter.

Various remineralization profiles can be derived from assumptions about particle degradability and sinking speed(s) (Suess, 1980; Martin et al., 1987; Middelburg, 1989;

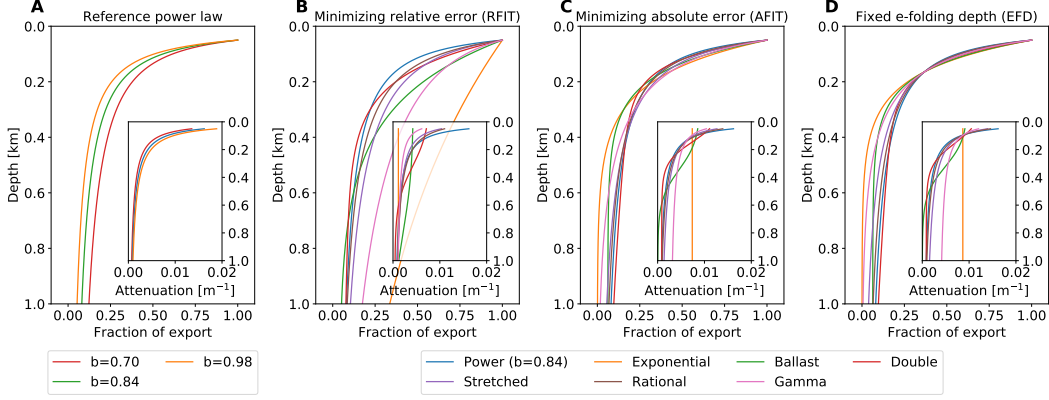


Figure 1. Fraction of sinking particulate organic matter exported from the 50 m surface layer remaining at each depth for (a) the reference power-law (Eq. 1) with exponents 0.84 ± 0.14 , and six alternative functions (Eq. S1–S6) fit to the reference power-law curve ($b=0.84$) by (b) statistically minimizing the relative error (“RFIT”), or (c) the absolute error (“AFIT”), and (d) matching the e-folding depth scale of 164 m (“EFD”). See Materials and Methods, Table S1 for fitting details, coefficients, and fit statistics. Inset plots show the attenuation rate of the export flux with depth $\left[\frac{1}{f} \frac{\partial f}{\partial z}, m^{-1}\right]$.

58 Banse, 1990; Armstrong et al., 2001; Lutz et al., 2002; Rothman & Forney, 2007; Kriest & Oschlies, 2008; Cael & Bisson, 2018). The ubiquitous “Martin Curve” (Martin et al., 1987) is a power-law profile (Eq. 1) that assumes slower-sinking and/or labile organic matter is preferentially depleted near the surface causing increasing sinking speed and/or remineralization timescale with depth (e.g. Kriest & Oschlies, 2011).

$$63 \quad f_p(z) = C_p z^{-b}, \quad (1)$$

64 where $f_p(z)$ is the fraction of the flux of particulate organic matter from a productive layer near the surface (Buesseler et al., 2020) sinking through the depth horizon z [m], 65 C_p [m^b] is a scaling coefficient, and b is a nondimensional exponent controlling how f_p 66 decreases with depth. Eq. 1 is often normalized to a reference depth z_o but this parameter is readily absorbed into C_p . 67 68

69 Considerable effort has been dedicated to determining value(s) for the exponent, 70 b (e.g., Martin et al., 1987, 1993; Berelson, 2001; Primeau, 2006; Kwon & Primeau, 2006; 71 Honjo et al., 2008; Henson et al., 2012; Kriest et al., 2012; Gloege et al., 2017; Wilson 72 et al., 2019). Open ocean particulate flux observations from the North Pacific (Martin

73 et al., 1987) indicate a b value of 0.858. Further analyses of expanded sediment trap datasets
74 suggest a possible range of approximately 0.84 ± 0.14 for the global b value (Martin et
75 al., 1993; Berelson, 2001; Primeau, 2006; Honjo et al., 2008; Gloege et al., 2017), though
76 a much wider range has been observed when including regional variability in b and optically-
77 and geochemically-derived flux estimates (Henson et al., 2012; Guidi et al., 2015; Pavia
78 et al., 2019). This may result from differences in temperature (Matsumoto, 2007), mi-
79 crobial community composition (Boyd & Newton, 1999), particle composition (Armstrong
80 et al., 2001), oxygen concentration (Devol & Hartnett, 2001), particle aggregation (Gehlen
81 et al., 2006; Schwinger et al., 2016; Niemeyer et al., 2019), or mineral ballasting (Gehlen
82 et al., 2006; Pabortsava et al., 2017).

83 Uncertainty in the value of b translates to uncertainty in the biological pump's im-
84 pact on the ocean carbon sink, atmosphere-ocean carbon partitioning, and climate model
85 projections. Thus, constraining b for the modern ocean and how it may differ in the past,
86 or the future, is of much interest from a climate perspective. Varying a global value of
87 b between 0.50–1.4 altered atmospheric $p\text{CO}_2$ by 86–185 μatm after several thousand years
88 of equilibration, in an influential modeling study (Kwon et al., 2009): Higher values of
89 b result in enhanced particle remineralization at shallower depths. Shallow watermasses
90 are more frequently ventilated, allowing remineralized CO_2 to be released back into the
91 atmosphere on shorter timescales. Due to this depth-dependence, a small change of degra-
92 dation depth can appreciably change atmospheric $p\text{CO}_2$ (Yamanaka & Tajika, 1996; Kwon
93 et al., 2009). Varying b over the plausible range in global values between 0.70–0.98 pro-
94 duces a more modest change in atmospheric $p\text{CO}_2$, over the range of $(-16,+12)\mu\text{atm}$ (Gloege
95 et al., 2017), while the modeled uncertainty in atmospheric $p\text{CO}_2$ associated with regional
96 variation in b is estimated between 5–15 μatm (Wilson et al., 2019).

97 Biogeochemical models are subject not only to parametric uncertainty (which value
98 for b and how b varies in space and time), but also structural uncertainty, i.e. which equa-
99 tion(s) to choose for the vertical flux of organic matter. The Martin Curve power-law
100 is an empirical fit to sediment trap data, but several other functional forms have also been
101 put forward (Suess, 1980; Middelburg, 1989; Banse, 1990; Armstrong et al., 2001; Lutz
102 et al., 2002; Dutkiewicz et al., 2005; Rothman & Forney, 2007; Marsay et al., 2015) that
103 fit sediment trap fluxes equivalently well and have equal if not better mechanistic jus-
104 tification (Cael & Bisson, 2018). Atmospheric $p\text{CO}_2$ and many other global biogeochem-
105 ical properties (Kwon & Primeau, 2006; Kriest et al., 2012; Aumont et al., 2017) will be

106 affected by this structural uncertainty, so it is critical to evaluate the impact of choos-
107 ing one remineralization profile “shape” over another.

108 We assess the effect of remineralization profile shape on biological pump strength
109 and evaluate a comprehensive estimate of structural uncertainty in terms of atmosphere-
110 ocean carbon partitioning in a global ocean biogeochemistry model. We substitute the
111 reference power-law curve for six plausible alternative remineralization profiles: expo-
112 nential (Banse, 1990; Dutkiewicz et al., 2005; Marsay et al., 2015; Gloege et al., 2017),
113 ballast (Armstrong et al., 2001; Gloege et al., 2017), double exponential (Lutz et al., 2002),
114 stretched exponential (Middelburg, 1989; Cael & Bisson, 2018), rational (Suess, 1980),
115 and upper incomplete gamma function of order zero (Rothman & Forney, 2007, we use
116 the shorthand “gamma function” for “upper incomplete gamma function of order zero”,
117 although different orders are possible). Each form corresponds to a basic mechanistic de-
118 scription of particle fluxes (Cael & Bisson, 2018), that we tightly constrained to the re-
119 ference profile by statistically minimizing export fraction misfits or by matching degra-
120 dation depth scales (Kwon et al., 2009). See Supporting Information for derivations of
121 these profiles.

122 These simulations indicate that structural uncertainty is an appreciable component,
123 around one third, of total uncertainty for understanding the biological pump (with the
124 remaining two thirds attributed to parametric uncertainty in b). Changing remineral-
125 ization functional form alters atmospheric $p\text{CO}_2$ by $\sim 10\text{-}15 \mu\text{atm}$ depending on how struc-
126 tural uncertainty is quantified, equivalent to ~ 0.08 uncertainty in a global value of the
127 power-law exponent, b , and similar to the uncertainty resulting from regional variation
128 of b .

129 Our results underscore the importance of characterizing basic mechanisms govern-
130 ing the biological pump. Furthermore, our results corroborate that depth-dependence
131 of these mechanisms is particularly important (Gehlen et al., 2006; Kriest & Oschlies,
132 2008): not only is biological pump-driven carbon export and storage an important con-
133 trol on atmospheric $p\text{CO}_2$, we find that rapidly decreasing particle degradation in the
134 upper ocean is equally important for a sufficient quantity of carbon to become isolated
135 in the deep ocean. While a given flux curve may be chosen for historical reasons or math-
136 ematical convenience, its skill should be compared to those of other idealized flux pro-
137 file parameterizations in Earth System Models used for projections of future climate.

138 2 Materials and Methods

139 2.1 Fitting the alternative remineralization curves.

140 We fit the alternative functions for export fluxes and remineralization (Fig. 1, Eq.
 141 S1–S6, see Supporting Information) to the reference power-law curve (Eq. 1) with the
 142 exponent $b=0.84$ using nonlinear regression on the model vertical grid to minimize the
 143 absolute curve mismatch (“ABS” simulations). Subsurface points were weighted equally
 144 (1.0), except for a heavily weighted top level (valued 1000, but the overall fit was largely
 145 insensitive to the choice of this value) to ensure all the profiles pass through the same
 146 value as the control profile, i.e. fraction of export from the productive surface layer is
 147 unity. We further matched the e-folding depth of remineralization to the reference (“EFD”
 148 simulations) by adding a second heavily weighted point to the reference power-law at 164 m
 149 depth ($z_0 e^{(1/b)}$), with an export fraction of e^{-1} . In a third set (“RFIT” simulations), the
 150 nonlinear regression is performed on the natural logarithm of the remineralization frac-
 151 tion in order to minimize the relative error of the reference profile match. Goodness of
 152 fit is evaluated by the Standard Error of Regression, \mathcal{S} , which is the sum of squared resid-
 153 uals, divided by statistical degrees of freedom (number of points minus number of pa-
 154 rameters). Coefficients and \mathcal{S} values for the eighteen curves are given in Table S1.

155 2.2 Numerical ocean biogeochemistry model.

156 Alternative remineralization profiles are substituted into global ocean simulations
 157 of a coarse resolution (2.8° , 15 vertical level) configuration of the Massachusetts Insti-
 158 tute of Technology general circulation model, MITgcm (Marshall et al., 1997), coupled
 159 to an idealized marine biogeochemistry model that considers the coupled cycles of dis-
 160 solved inorganic carbon, alkalinity, phosphate, dissolved organic phosphorus, oxygen, and
 161 dissolved iron (Dutkiewicz et al., 2006; Parekh et al., 2005, 2006).

162 Two-thirds of surface net community production (which depends on light, phos-
 163 phate, and iron using Michaelis-Menten kinetics) is channelled into dissolved organic mat-
 164 ter that is largely remineralized in the surface ocean with a timescale of 6 months (Yamanaka
 165 & Tajika, 1997), while one-third is exported to the ocean interior via sinking particu-
 166 late organic matter subject to depth-dependent remineralization rates. Elemental bio-
 167 logical transformations are related using fixed stoichiometric ratios $R_{C:N:P:Fe:O_2} = 117 :$
 168 $16 : 1 : 4.68 \times 10^{-4} : -170$ (Anderson & Sarmiento, 1994) with a prescribed inorganic

169 to organic rain ratio of 7% (Yamanaka & Tajika, 1996). The total atmosphere-ocean car-
 170 bon inventory is conserved as there is no riverine carbon input or sediment carbon burial,
 171 which may impact the model’s transient behavior and steady state (Roth et al., 2014).
 172 Atmosphere-ocean exchange of CO₂ captures the magnitude and variation of observed
 173 air-sea fluxes (Lauderdale et al., 2016).

174 Our model includes tracers to separate the *in situ* concentrations of carbon into:
 175 (i) a component subducted from the surface layer and transported conservatively by ocean
 176 circulation (the “preformed” carbon concentration, C_{pre}), and (ii) a component that in-
 177 tegrates export and remineralization of sinking particles as a watermass transits the ocean
 178 interior (the “biological” carbon concentration, C_{bio}), which encompasses both soft tis-
 179 sue regeneration and carbonate dissolution, and connects more directly to the biolog-
 180 ical pump (Volk & Hoffert, 1985; Ito & Follows, 2005). We integrate simulations for 10,000
 181 years toward steady state in atmosphere-ocean carbon partitioning.

182 **3 Results**

183 **3.1 Varying the exponent of the reference power-law curve.**

184 Global power-law exponent, b , estimates range from 0.70 (Primeau, 2006) based
 185 on sediment traps to ~ 1.00 based on inverse models fit to tracer distributions (Kwon &
 186 Primeau, 2006, 2008; Kwon et al., 2009; Kriest et al., 2012). These values match the global
 187 b interquartile range of 0.70–0.98 in (Gloege et al., 2017). We integrate three simulations
 188 with $b = 0.84 \pm 0.14$ (Fig. 1a) using the standard power-law parameterization (Eq. 1)
 189 to produce a baseline estimate of biological pump parametric uncertainty. The reference
 190 simulation has the exponent $b=0.84$.

191 Higher b values cause the fraction of sinking particulate matter to decrease faster
 192 with depth, that is, attenuation ($1/f_p \cdot \partial f_p / \partial z$) is higher in the upper ocean, whereas
 193 lower exponents have less attenuation and a larger proportion of export reaching the deep
 194 ocean (Figs. 1a and S2a–f). A negative feedback occurs near the surface in our simula-
 195 tions. For example, when b is increased, higher rates of upper ocean attenuation cause
 196 an increase in surface nutrient availability, and therefore more overall biological produc-
 197 tion (see ΔB_C , Table S2). Local biological activity enhancement increases local rates of
 198 particle export, evaluated by integrated fluxes through the deepest mixed layer depth
 199 (ΔE_{mld} , Table S2). However, higher shallow export is compensated by greater upper ocean

200 remineralization, due to larger exponent value, resulting instead in reduced export flux
 201 anomalies through 1 km depth (ΔE_{1km} , Table S2), and vice versa when b is decreased
 202 (e.g. global experiments in Kriest & Oschlies, 2011). The global ocean reservoir of bi-
 203 ological carbon changes proportionally with ΔE_{1km} (Figs. 2a, blue symbols, S2g-l, and
 204 ΔC_{bio} , Table S2) and inversely-proportional to ΔE_{mld} (Fig. S3a).

205 **3.2 Impact of alternative remineralization curve shape.**

206 Generally speaking, the six alternative remineralization profiles (Eq. S1–S6) ob-
 207 jectively characterized by statistically fitting parameters to match the reference power-
 208 law curve ($b=0.84$) do reproduce similar sinking particle remineralization rates (Fig. 1b–
 209 d). This is perhaps not a surprise, since we would not consider these functions to be plau-
 210 sible alternatives to the Martin Curve if they could not describe export fluxes at least
 211 as well as a power-law.

212 Nevertheless, the simple exponential and gamma function curves do not fit the ref-
 213 erence power-law profile as well as the other functions (Fig. 1b–d) because these profiles
 214 cannot capture a strong depth-change in remineralization. Simulations with lower-attenuation
 215 profiles result in increased export fluxes (Fig. S4), and vice versa, as with the simula-
 216 tions varying b (Fig. 2a). These particulate flux anomalies translate into changes in the
 217 distribution of biological carbon, with positive export flux anomalies through the 1 km
 218 depth horizon (ΔE_{1km}) corresponding to increase in the biological carbon pool (C_{bio} ,
 219 Fig. 2a), while negative export flux anomalies result in lower biological carbon concen-
 220 trations. For instance, in RFIT simulations, the exponential and gamma function pro-
 221 files show an increase in 1 km export fluxes and biological carbon storage, while the re-
 222 verse occurs for exponential and gamma profiles in AFIT and EFD simulations. Geo-
 223 graphically, stronger ocean interior sinking fluxes tend to redistribute biological carbon
 224 into the Southern Ocean and deep North Pacific at the expense of the North Atlantic
 225 (Fig. S5–S7), while shallower remineralization tends to increase North Atlantic biologi-
 226 cal carbon concentrations whilst decreasing concentrations in the Southern Ocean and
 227 deep North Pacific. This is a reflection of the accumulation of C_{bio} as a water mass tran-
 228 sits the global meridional overturning circulation with the oldest waters upwelling in the
 229 Southern Ocean and North Pacific (Kwon & Primeau, 2006; Kriest & Oschlies, 2011; Kri-
 230 est et al., 2012; Romanou et al., 2014). The ballast profile has a more complex distri-
 231 bution of biological carbon anomalies in surface, intermediate, and deep waters such that

232 the relationship between export flux and ΔC_{bio} is better captured by considering deeper
 233 horizons (e.g. green symbols in Fig. 2a at the 1 km horizon, versus 2 km in Fig. S3b).

234 **3.3 Evaluating structural uncertainty of the biological pump.**

235 Altering the strength of the biological pump leads to changes in air-sea carbon bal-
 236 ance. The reference simulation has a steady-state atmospheric $p\text{CO}_2$ of $269.3 \mu\text{atm}$. In-
 237 creasing b from 0.70 to 0.98 increases $p\text{CO}_2$ by $46.36 \mu\text{atm}$ in this model (range: -21.6 –
 238 $24.8 \mu\text{atm}$, wide grey bars in Fig. 2b, Table S2). This is higher than the “nutrient restor-
 239 ing” case in Kwon et al. (2009), but lower than their “constant export” case, consistent
 240 with our model’s dynamic biological productivity response.

241 Alternative profiles with reduced export flux through 1 km and reduced biological
 242 carbon storage result in increased atmospheric $p\text{CO}_2$, and vice versa (Fig. 2b, Table S3).
 243 The double exponential function has the most free parameters (four) and therefore fits
 244 the power-law extremely well, producing small differences in atmospheric $p\text{CO}_2$ (less than
 245 $2 \mu\text{atm}$). The rational function also agrees well, but could produce larger anomalies if
 246 the reference profile’s b -value was further from 1.00, i.e. 0.70. Stretched exponential and
 247 ballast curves produce moderate changes in atmospheric $p\text{CO}_2$ but are generally smaller
 248 than, or similar to, the 0.14 changes in b for the power-law curves (Fig. 2b). However,
 249 the simple exponential and gamma function anomalies clearly deviate from the other sim-
 250 ulations, with greater biological carbon concentrations and drawdown of atmospheric CO_2
 251 for the RFIT simulations, and the inverse for AFIT and EFD simulations. Export fluxes
 252 and remineralization are significantly different in the upper ocean for these parameter-
 253 izations, which can be explained by their largely invariant attenuation rates with depth
 254 (Fig. 1 insets): simple exponential and gamma parameterizations cannot have both short
 255 remineralization lengthscales in the upper ocean and long remineralization lengthscales
 256 in the deep ocean.

257 There are multiple ways to compare parametric and structural uncertainty quan-
 258 titatively. Parametric uncertainty is found by varying the power-law exponent within
 259 its plausible global range ($b = 0.84 \pm 0.14$), producing absolute atmospheric $p\text{CO}_2$ anoma-
 260 lies of 21.6 – $24.8 \mu\text{atm}$ (Fig. 2b, Table S3). For structural uncertainty, the median change
 261 in absolute atmospheric $p\text{CO}_2$ is $12.47 \pm 10.67 \mu\text{atm}$ (b -anomaly equivalent of 0.07 ± 0.06)
 262 across all simulations with alternate functional forms. We choose the median \pm median

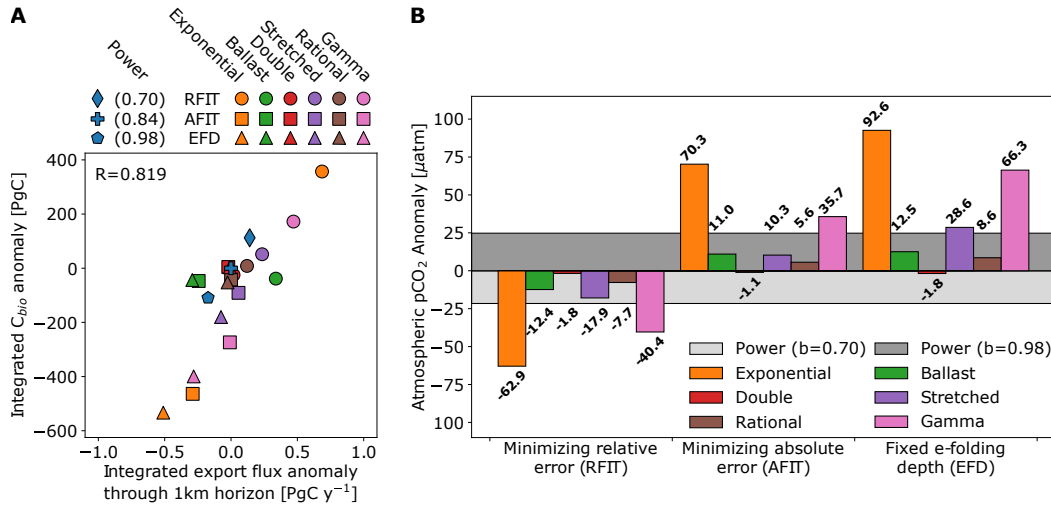


Figure 2. Impact of alternative remineralization curve shape on the air-sea carbon balance (a) change in the integrated export flux rate [$PgC\ y^{-1}$] passing through the 1 km depth level against integrated biological carbon reservoir anomaly [PgC], both with respect to the power-law ($b=0.84$). Three power-law simulations ($b=0.84\pm 0.14$) are indicated by the blue symbols (diamond, cross, and pentagon), circle, square, and triangle symbols indicate that profile coefficients (Eq. S1–S6) were derived by minimizing the relative fit error (“RFIT”), minimizing the absolute fit error (“AFIT”), and fixing the e-folding depth of remineralization (“EFD”) respectively, (b) atmospheric pCO_2 anomalies (μatm) for remineralization profiles with respect to the reference power-law ($b=0.84$) for power-law exponent values $b=0.70$ and 0.98 , and statistical fits of alternative profiles “RFIT” (left), “AFIT” (middle), and “EFD” (right). Values are given in Tables S2 and S3.

263 absolute deviation so that our result is robust to large anomalies associated with sim-
 264 ple exponential and gamma functional forms. For RFIT, AFIT, and EFD simulations
 265 separately, the medians are 15.15 ± 10.40 , 10.65 ± 7.30 , and $20.57 \pm 15.37 \mu\text{atm}$, respectively,
 266 giving a $15.15 \pm 4.51 \mu\text{atm}$ grand median (b -anomaly equivalent of 0.09 ± 0.03). Exclud-
 267 ing profiles with largely invariant attenuation rates with depth, i.e. exponential and gamma
 268 function profiles, the overall medians for RFIT, AFIT, and EFD are 10.07 ± 2.32 , 7.96 ± 2.69 ,
 269 and $10.57 \pm 1.98 \mu\text{atm}$, respectively, with a $10.07 \pm 0.50 \mu\text{atm}$ grand median (b -anomaly
 270 equivalent of 0.06 ± 0.00). In summary, our results are largely robust, indicating a struc-
 271 tural uncertainty of $10\text{--}15 \mu\text{atm}$, roughly half of parametric uncertainty for the biolog-
 272 ical pump ($22\text{--}25 \mu\text{atm}$, $b = 0.84 \pm 0.14$), analogous to a ~ 0.08 change in b .

273 **3.4 Role of nonlinearity in the biological pump.**

274 Much emphasis is placed on the biological pump’s effect on climate by significantly
 275 lowering atmospheric CO_2 levels, but our exponential and gamma function simulations
 276 indicate that having a biological pump (i.e. uptake, export, and depth-dependent rem-
 277 ineralization) and an associated biological carbon store is not necessarily sufficient to pro-
 278 duce atmospheric carbon drawdown of the expected magnitude, such as a $\sim 200 \mu\text{atm}$ dif-
 279 ference between biotic and abiotic oceans (Volk & Hoffert, 1985). To understand what
 280 aspects of the biological pump are important for significantly lowering atmospheric CO_2 ,
 281 we ran a simulation (“NOPOM”) that represents a hypothetical ocean with no partic-
 282 ulate organic matter export and without a biological carbon pool. Instead, biological pro-
 283 duction is channelled into dissolved organic matter that is remineralized near the sur-
 284 face.

285 Atmospheric pCO_2 in NOPOM increases $165.4 \mu\text{atm}$ (Table S2) with respect to our
 286 reference power-law: slightly less outgassing than Volk and Hoffert (1985), but the NOPOM
 287 ocean does have biological activity and a dissolved organic carbon store. This is roughly
 288 twice as large as the outgassing resulting from the use of a simple exponential reminer-
 289 alization profile fit to the reference power-law curve in AFIT and EFD simulations (70.3
 290 and $92.6 \mu\text{atm}$), despite these simulations supporting significant 1 km export fluxes (1.460
 291 and 1.238 PgC y^{-1} , only 20% less than the reference power law) as well as large stores
 292 of biological carbon (1830 and 1900 PgC , compared to 176 PgC for NOPOM). Thus, only
 293 about half of the biological pump’s effect on atmosphere-ocean carbon drawdown ($\sim 80 \mu\text{atm}$)

294 can be attributed to export of particulate organic matter and biological carbon storage
295 (Fig. S8).

296 The remaining $\sim 80 \mu\text{atm}$ drawdown in atmospheric carbon content is due to the
297 change in shape of remineralization curves between a biological pump represented by AFIT
298 and EFD exponential curves compared to a biological pump represented by the refer-
299 ence power-law profile. Exponential profiles have a constant rate of change of reminer-
300 alization, or attenuation of the sinking particle flux with depth (Fig. 1c and d, insets),
301 which results in the majority of the sinking particle flux from the surface ocean being
302 remineralized in the upper 2 km: export fluxes through this horizon are 0.204 and 0.140
303 PgC y^{-1} . Alternatively, attenuation for the power-law curve decreases significantly with
304 depth leading to a substantial 2 km export flux of 0.802 PgC y^{-1} . Thus, for AFIT and
305 EFD exponential profiles, there is very little abyssal biological carbon storage to act as
306 a long-term reservoir of atmospheric CO_2 , whereas rapidly decreasing attenuation in the
307 reference power-law supports long-term biological carbon storage.

308 In other words, decreasing upper ocean particle attenuation, or increasing reminer-
309 alization lengthscale with depth, appears to be equally important for air-sea carbon par-
310 titioning as export and storage of biological carbon (Fig. S8).

311 4 Discussion and Conclusions

312 Atmospheric CO_2 levels are intimately tied to the strength of the ocean's biolog-
313 ical pump (Volk & Hoffert, 1985; Ito & Follows, 2005), comprising linked processes of
314 primary production, export of organic matter from the upper ocean, and the degrada-
315 tion of particles back to inorganic constituents with depth. The challenge of measuring
316 particulate fluxes via sediment traps, optical proxies, or geochemical methods (Martin
317 et al., 1987; Berelson, 2001; Honjo et al., 2008; Henson et al., 2012; Guidi et al., 2015;
318 Pavia et al., 2019), the spatiotemporal variability of fluxes, and the complexity of the
319 governing mechanisms introduce uncertainty into representation of the biological pump
320 in ocean biogeochemistry, ecosystem, and climate models. We explored the impact of struc-
321 tural uncertainty—remineralization profile shape—on atmosphere-ocean carbon parti-
322 tioning, using seven mechanistically-distinct functional forms of particulate organic mat-
323 ter flux that capture observational spread equivalently well (Cael & Bisson, 2018). Steady-
324 state atmospheric pCO_2 is inversely related to the biological carbon pool, thus profiles

325 with more efficient export through 1 km, and greater biological carbon storage, lead to
326 atmospheric CO₂ drawdown.

327 In our model, a 0.14 change in the power-law exponent, b , results in a 22–25 μatm
328 change in atmospheric pCO₂, indicating that structural uncertainty revealed by our sim-
329 ulations of 10–15 μatm is equivalent to ~ 0.08 change in the global b value. Thus struc-
330 tural uncertainty is roughly half the size of parameteric uncertainty, making it a substan-
331 tial one-third contribution to our overall estimate of total uncertainty (the sum of struc-
332 tural and parametric uncertainties) in understanding the biological pump. In addition
333 our result is in the upper range of the 5–15 μatm uncertainty associated with regional
334 variation in b (Wilson et al., 2019).

335 Historically, the focus been on remineralization lengthscale (Kwon et al., 2009), but
336 our results imply that multiple lengthscales of attenuation are critical to the biological
337 pump’s global impact, indicating that vertical gradient in attenuation is a first-order con-
338 trol on climate. The simple exponential functional form, with constant depth attenua-
339 tion, results in much larger atmospheric pCO₂ anomalies of $\sim 80\mu\text{atm}$ for AFIT and EFD
340 simulations, despite being statistically fit to be as similar to the reference power law as
341 possible (also the case for for gamma function profiles). This is roughly half the $\sim 165\mu\text{atm}$
342 increase that results from removing the biological pump altogether (NOPOM), highlight-
343 ing the importance for the air-sea carbon balance, not only of the existence of a biolog-
344 ical pump that maintains interior ocean biological carbon stores (Volk & Hoffert, 1985),
345 but also its non-linearity (Fig. S8). More specifically, significant decrease of attenuation
346 with depth is a key factor in the biological pump’s modulation of atmospheric CO₂ lev-
347 els. Even when the exponential profiles’ parameters are determined by matching the e-
348 folding remineralization depth of the reference power-law curve (Kwon et al., 2009), the
349 result is still large atmospheric pCO₂ anomalies caused by largely invariant attenuation
350 rates with depth.

351 Our study evaluates structural uncertainty in the ocean’s biological pump in a sys-
352 tematic way. Although previous studies have compared individual, or a subset, of the
353 alternative remineralization curves used here (e.g., Yamanaka & Tajika, 1996; Gehlen
354 et al., 2006; Kriest & Oschlies, 2008; Schwinger et al., 2016; Gloege et al., 2017; Niemeier
355 et al., 2019; Kriest et al., 2020) with a focus on minimizing model-observational differ-
356 ences, none has attempted to evaluate this structural uncertainty by just changing the

357 shape of the remineralization profile, which we do here by comparing six alternative func-
358 tional forms statistically fit in three different ways to a reference power-law profile. De-
359 spite these profile choices resulting in non-negligible differences in ocean biogeochemi-
360 cal distributions (Kriest et al., 2012; Aumont et al., 2017) and atmospheric CO₂ levels
361 (Kwon et al., 2009), comparison of model output to climatological data (Garcia et al.,
362 2014) does not significantly change (Fig. S9), such that all the curves still quantitatively
363 reproduce the observations to a similar degree.

364 As Earth System Models continue to rely on simple biological pump parameter-
365 izations, our estimate of structural uncertainty underscores the importance of research
366 aimed at improving the basic mechanistic characterization of the biological pump (Boyd
367 et al., 2019), and particularly the depth-dependence or evolution of these mechanisms.
368 One such improvement is to consider the spectrum of sinking particle properties, such
369 as size (Schwinger et al., 2016; Niemeier et al., 2019), sinking speeds (Kriest & Oschlies,
370 2008) or material lability (Aumont et al., 2017), and how they effect export fluxes. These
371 studies often derive components that rely on upper and lower incomplete gamma func-
372 tions, as well as gamma distributions, but ultimately do not produce gamma function
373 flux profiles. The Rothman and Forney (2007) profile (Eqn. S6) is a special case of the
374 upper incomplete gamma function (where the order, $a=0$). However, statistical fits of
375 integer orders of the upper incomplete gamma function where $a>0$ to the reference power-
376 law ($b=0.84$) are poor (See Fig. S1, including the simple exponential curve, which is pro-
377 portional to an upper incomplete gamma function of order $a=1$), and as stand-alone rem-
378 ineralization parameterizations may include particle classes whose remineralization pro-
379 files may not exist in the ocean. On the other hand, a more general three-parameter up-
380 per incomplete gamma function parameterization, $C_g\Gamma(a_g, z/\ell_g)$, fits the Martin curve
381 very well with $a_g\approx-0.8$ (Fig. S1), and would correspond to a constant-sinking reactiv-
382 ity continuum model (Aumont et al., 2017) with a power-law reactivity distribution. How-
383 ever, reactivity continuum models do not describe reactivity using a power law, and
384 instead use lighter-tailed distributions such as the gamma (Boudreau & Ruddick, 1991),
385 beta (Vähätalo et al., 2010), or log-normal distribution (Forney & Rothman, 2012). Thus
386 we did not include these additional profiles in our biological pump structural error en-
387 semble as there is not a justifiable basis for $a>1$, nor a plausible mechanism for $a<0$, un-
388 like the six alternative remineralization curves presented.

389 A better process-based understanding is critical to choosing between these param-
390 eterizations based on their mechanistic underpinnings and thus reducing structural un-
391 certainty, because empirical fits to flux measurements alone cannot currently do so (Gehlen
392 et al., 2006; Cael & Bisson, 2018). Indeed, there are also no guarantees that more ex-
393 tensively sampled ocean nutrient distributions are able to distinguish between the per-
394 formance of idealized and more explicit remineralization schemes either (Niemeyer et al.,
395 2019; Schwinger et al., 2016).

396 In our simulations, the parameterizations were forced to be as similar as possible
397 with regard to the three different criteria (minimizing misfit error or matching the ref-
398 erence e-folding depth of remineralization), but functional forms based on different pro-
399 cesses will have different sensitivities to temperature and other phenomena, and there-
400 fore will produce divergent projections and different climate feedbacks. Furthermore, each
401 alternative functional form will be associated with its own parametric uncertainty. Un-
402 fortunately, significantly less is known about the natural range of parameters associated
403 with the alternative remineralization profiles in the real ocean, because they have not
404 been used as widely as the Martin Curve.

405 There are other factors that could affect the distribution, export, and depth de-
406 pendent remineralization of sinking particles, and therefore ocean carbon sink/atmospheric
407 CO₂ sensitivity, that we held the same between simulations. For example, our assump-
408 tion of a closed carbon cycle with no sediment burial or riverine fluxes may underesti-
409 mate the biological pump effect on atmospheric CO₂ for the different remineralization
410 profiles by 4–7 times (Roth et al., 2014) on timescales of 10–100 thousand years. Between
411 different models, the overall strength of the deep ocean carbon store may be more de-
412 pendent on remineralization profile parameters than on different ocean circulations, al-
413 though circulation impact on upper ocean production would modify the overall relation-
414 ships shown here (Romanou et al., 2014; Kriest et al., 2020). Vertical grid resolution and
415 numerical diffusion might also result in changes to the ocean carbon sink (Kriest & Os-
416 chlies, 2011), although again these changes may not manifest in the short timespan that
417 many more complex coupled ocean-ecosystems are integrated for (Kwon et al., 2009; Schwinger
418 et al., 2016). Despite these challenges, it would be valuable to compare these different
419 functional forms within state-of-the-art Earth System Models, either directly or via im-
420 plied remineralization profile shape, to improve confidence in projections involving biosphere-
421 climate interactions.

422 **Acknowledgments**

423 We thank two anonymous reviewers for their comments and suggestions, and Lauren Hinkel
424 (MIT) for copyediting and clarity advice on previous drafts of this manuscript. **Fund-**
425 **ing:** JML was supported by the US National Science Foundation (“Dust PIRE”, 1545859);
426 BBC was supported by a Simons Postdoctoral Fellowship in Marine Microbial Ecology,
427 the UK National Environmental Research Council (NE/R015953/1), and the EU H2020
428 project COMFORT (820989). This work reflects only the authors’ views; the European
429 Commission and their executive agency are not responsible for any use that may be made
430 of the information the work contains. **Author contributions:** JML and BBC contributed
431 equally to simulation design, analysis, interpretation, and manuscript preparation. **Com-**
432 **peting interests:** The authors declare no competing interests. **Data availability:** Pre-
433 liminary model input, code, and output processing routines can be accessed via GitHub
434 (https://github.com/seamanticscience/Lauderdale_and_Cael_Exports, to be updated and
435 uploaded to *Zenodo.org* open science archive and doi provided here).

References

- 436
437 Anderson, L. A., & Sarmiento, J. L. (1994). Redfield ratios of remineralization de-
438 termined by nutrient data analysis. *Global Biogeochem. Cycles*, *8*, 65–80.
- 439 Armstrong, R. A., Lee, C., Hedges, J. I., Honjo, S., & Wakeham, S. G. (2001). A
440 new, mechanistic model for organic carbon fluxes in the ocean based on the
441 quantitative association of poc with ballast minerals. *Deep Sea Res. Part II*,
442 *49*(1), 219–236. doi: 10.1016/S0967-0645(01)00101-1
- 443 Aumont, O., van Hulst, M., Roy-Barman, M., Dutay, J. C., Éthé, C., & Gehlen,
444 M. (2017). Variable reactivity of particulate organic matter in a global
445 ocean biogeochemical model. *Biogeosciences*, *14*(9), 2321–2341. doi:
446 10.5194/bg-14-2321-2017
- 447 Banse, K. (1990). New views on the degradation and disposition of organic parti-
448 cles as collected by sediment traps in the open sea. *Deep Sea Research Part A*.
449 *Oceanographic Research Papers*, *37*(7), 1177–1195. doi: 10.1016/0198-0149(90)
450 90058-4
- 451 Berelson, W. M. (2001). The flux of particulate organic carbon into the ocean in-
452 terior: A comparison of four U.S. JGOFS regional studies. *Oceanography*, *14*,
453 59–67. doi: 10.5670/oceanog.2001.07
- 454 Boudreau, B. P., & Ruddick, B. R. (1991). On a reactive continuum representation
455 of organic matter diagenesis. *American Journal of Science*, *291*(5), 507. doi:
456 10.2475/ajs.291.5.507
- 457 Boyd, P. W., Claustre, H., Levy, M., Siegel, D. A., & Weber, T. (2019). Multi-
458 faceted particle pumps drive carbon sequestration in the ocean. *Nature*,
459 *568*(7752), 327–335. doi: 10.1038/s41586-019-1098-2
- 460 Boyd, P. W., & Newton, P. P. (1999). Does planktonic community structure deter-
461 mine downward particulate organic carbon flux in different oceanic provinces?
462 *Deep Sea Res. Part I*, *46*(1), 63–91. doi: 10.1016/S0967-0637(98)00066-1
- 463 Buesseler, K. O., Boyd, P. W., Black, E. E., & Siegel, D. A. (2020). Metrics that
464 matter for assessing the ocean biological carbon pump. *Proc. Nat. Acad. Sci.*,
465 *117*(18), 9679. doi: 10.1073/pnas.1918114117
- 466 Cael, B. B., & Bisson, K. (2018). Particle flux parameterizations: Quantitative and
467 mechanistic similarities and differences. *Front. Mar. Sci.*, *5*, 395. doi: 10.3389/
468 fmars.2018.00395

- 469 Devol, A. H., & Hartnett, H. E. (2001). Role of the oxygen-deficient zone in transfer
470 of organic carbon to the deep ocean. *Limnol. Oceanogr.*, *46*(7), 1684–1690. doi:
471 10.4319/lo.2001.46.7.1684
- 472 Dutkiewicz, S., Follows, M. J., Heimbach, P., & Marshall, J. (2006). Controls on
473 ocean productivity and air–sea carbon flux: An adjoint model sensitivity study.
474 *Geophys. Res. Lett.*, *33*. doi: 10.1029/2005GL024987
- 475 Dutkiewicz, S., Follows, M. J., & Parekh, P. (2005). Interactions of the iron and
476 phosphorus cycles: A three dimensional model study. *Global Biogeochem. Cy-*
477 *cles*, *19*. doi: 10.1029/2004GB002342
- 478 Forney, D. C., & Rothman, D. H. (2012). Common structure in the heterogeneity of
479 plant-matter decay. *Journal of The Royal Society Interface*, *9*(74), 2255–2267.
480 doi: 10.1098/rsif.2012.0122
- 481 Garcia, H. E., Locarnini, R. A., Boyer, T. P., Antonov, J. I., Baranova, O., Zweng,
482 M., . . . Johnson, D. (2014). World Ocean Atlas 2013, volume 4: Dissolved
483 inorganic nutrients (phosphate, nitrate, silicate). In S. Levitus & A. Mishonov
484 (Eds.), *NOAA Atlas NESDIS 76* (p. 25pp.).
- 485 Gehlen, M., Bopp, L., Emprin, N., Aumont, O., Heinze, C., & Ragueneau, O.
486 (2006). Reconciling surface ocean productivity, export fluxes and sediment
487 composition in a global biogeochemical ocean model. *Biogeosciences*, *3*(4),
488 521–537. doi: 10.5194/bg-3-521-2006
- 489 Gloege, L., McKinley, G. A., Mouw, C. B., & Ciochetto, A. B. (2017). Global eval-
490 uation of particulate organic carbon flux parameterizations and implications
491 for atmospheric pCO₂. *Global Biogeochem. Cycles*, *31*(7), 1192–1215. doi:
492 10.1002/2016GB005535
- 493 Guidi, L., Legendre, L., Reygondeau, G., Uitz, J., Stemmann, L., & Henson, S. A.
494 (2015). A new look at ocean carbon remineralization for estimating deep-
495 water sequestration. *Global Biogeochem. Cycles*, *29*(7), 1044–1059. doi:
496 10.1002/2014GB005063
- 497 Henson, S. A., Sanders, R., & Madsen, E. (2012). Global patterns in efficiency of
498 particulate organic carbon export and transfer to the deep ocean. *Global Bio-*
499 *geochem. Cycles*, *26*(1). doi: 10.1029/2011GB004099
- 500 Honjo, S., Manganini, S. J., Krishfield, R. A., & Francois, R. (2008). Particulate
501 organic carbon fluxes to the ocean interior and factors controlling the biolog-

- 502 ical pump: A synthesis of global sediment trap programs since 1983. *Prog.*
503 *Oceanogr.*, *76*(3), 217–285. doi: 10.1016/j.pocean.2007.11.003
- 504 Ito, T., & Follows, M. J. (2005). Preformed phosphate, soft tissue pump and atmo-
505 spheric CO₂. *J. Mar. Res.*, *63*, 813–839.
- 506 Kriest, I., Kähler, P., Koeve, W., Kvale, K., Sauerland, V., & Oeschles, A. (2020).
507 One size fits all? calibrating an ocean biogeochemistry model for different cir-
508 culations. *Biogeosciences*, *17*(12), 3057–3082. doi: 10.5194/bg-17-3057-2020
- 509 Kriest, I., & Oeschles, A. (2008). On the treatment of particulate organic matter
510 sinking in large-scale models of marine biogeochemical cycles. *Biogeosciences*,
511 *5*(1), 55–72. doi: 10.5194/bg-5-55-2008
- 512 Kriest, I., & Oeschles, A. (2011). Numerical effects on organic-matter sedimentation
513 and remineralization in biogeochemical ocean models. *Ocean Model.*, *39*(3),
514 275–283. doi: 10.1016/j.ocemod.2011.05.001
- 515 Kriest, I., Oeschles, A., & Khatiwala, S. (2012). Sensitivity analysis of simple global
516 marine biogeochemical models. *Global Biogeochem. Cycles*, *26*(2). doi: 10
517 .1029/2011GB004072
- 518 Kwon, E. Y., & Primeau, F. (2006). Optimization and sensitivity study of a bio-
519 geochemistry ocean model using an implicit solver and in situ phosphate data.
520 *Global Biogeochem. Cycles*, *20*(4). doi: 10.1029/2005GB002631
- 521 Kwon, E. Y., & Primeau, F. (2008). Optimization and sensitivity of a global biogeo-
522 chemistry ocean model using combined in situ DIC, alkalinity, and phosphate
523 data. *J. Geophys. Res.*, *113*(C8). doi: 10.1029/2007JC004520
- 524 Kwon, E. Y., Primeau, F., & Sarmiento, J. L. (2009). The impact of remineraliza-
525 tion depth on the air–sea carbon balance. *Nature Geosci.*, *2*(9), 630–635. doi:
526 10.1038/ngeo612
- 527 Lauderdale, J. M., Dutkiewicz, S., Williams, R. G., & Follows, M. J. (2016). Quan-
528 tifying the drivers of ocean-atmosphere CO₂ fluxes. *Global Biogeochem. Cycles*,
529 *30*(7), 983–999. doi: 10.1002/2016GB005400
- 530 Lutz, M., Dunbar, R., & Caldeira, K. (2002). Regional variability in the vertical flux
531 of particulate organic carbon in the ocean interior. *Global Biogeochem. Cycles*,
532 *16*(3), 11–11–18. doi: 10.1029/2000GB001383
- 533 Marsay, C. M., Sanders, R. J., Henson, S. A., Pabortsava, K., Achterberg, E. P.,
534 & Lampitt, R. S. (2015). Attenuation of sinking particulate organic carbon

- 535 flux through the mesopelagic ocean. *Proc. Nat. Acad. Sci.*, *112*(4), 1089. doi:
536 10.1073/pnas.1415311112
- 537 Marshall, J., Adcroft, A., Hill, C., Perelman, L., & Heisey, C. (1997). A finite-
538 volume, incompressible Navier Stokes model for studies of the ocean on parallel
539 computers. *J. Geophys. Res.*, *102*(C3), 5753–5766.
- 540 Martin, J. H., Fitzwater, S. E., Michael Gordon, R., Hunter, C. N., & Tanner, S. J.
541 (1993). Iron, primary production and carbon-nitrogen flux studies during the
542 jgofs north atlantic bloom experiment. *Deep Sea Res. Part II*, *40*(1), 115–134.
543 doi: 10.1016/0967-0645(93)90009-C
- 544 Martin, J. H., Knauer, G. A., Karl, D. M., & Broenkow, W. W. (1987). Vertex: car-
545 bon cycling in the northeast pacific. *Deep-Sea Res.*, *34*(267–285).
- 546 Matsumoto, K. (2007). Biology-mediated temperature control on atmospheric
547 pCO₂ and ocean biogeochemistry. *Geophys. Res. Lett.*, *34*(20). doi:
548 10.1029/2007GL031301
- 549 Middelburg, J. J. (1989). A simple rate model for organic matter decomposition
550 in marine sediments. *Geochim. Cosmochim. Acta*, *53*(7), 1577–1581. doi: 10
551 .1016/0016-7037(89)90239-1
- 552 Niemeyer, D., Kriest, I., & Oschlies, A. (2019). The effect of marine ag-
553 gregate parameterisations on nutrients and oxygen minimum zones in a
554 global biogeochemical model. *Biogeosciences*, *16*(15), 3095–3111. doi:
555 10.5194/bg-16-3095-2019
- 556 Pabortsava, K., Lampitt, R. S., Benson, J., Crowe, C., McLachlan, R., Le Moigne,
557 F. A. C., ... Woodward, E. M. S. (2017). Carbon sequestration in the deep
558 atlantic enhanced by saharan dust. *Nature Geosci.*, *10*(3), 189–194. doi:
559 10.1038/ngeo2899
- 560 Parekh, P., Follows, M. J., & Boyle, E. A. (2005). Decoupling of iron and
561 phosphate in the global ocean. *Global Biogeochem. Cycles*, *19*. doi:
562 10.1029/2004GB002280
- 563 Parekh, P., Follows, M. J., Dutkiewicz, S., & Ito, T. (2006). Physical and biological
564 regulation of the soft tissue carbon pump. *Paleoceanography*, *21*. doi: 10.1026/
565 2005PA001258
- 566 Pavia, F. J., Anderson, R. F., Lam, P. J., Cael, B. B., Vivancos, S. M., Fleisher,
567 M. Q., ... Edwards, R. L. (2019). Shallow particulate organic carbon regen-

- 568 eration in the south pacific ocean. *Proc. Nat. Acad. Sci.*, *116*(20), 9753. doi:
569 10.1073/pnas.1901863116
- 570 Primeau, F. (2006). On the variability of the exponent in the power law depth
571 dependence of poc flux estimated from sediment traps. *Deep Sea Res. Part I*,
572 *53*(8), 1335–1343. doi: 10.1016/j.dsr.2006.06.003
- 573 Romanou, A., Romanski, J., & Gregg, W. W. (2014). Natural ocean carbon cy-
574 cle sensitivity to parameterizations of the recycling in a climate model. *Biogeo-*
575 *sciences*, *11*(4), 1137–1154. doi: 10.5194/bg-11-1137-2014
- 576 Roth, R., Ritz, S. P., & Joos, F. (2014). Burial-nutrient feedbacks amplify the
577 sensitivity of atmospheric carbon dioxide to changes in organic matter reminer-
578 alisation. *Earth Syst. Dynam.*, *5*(2), 321–343. doi: 10.5194/esd-5-321-2014
- 579 Rothman, D. H., & Forney, D. C. (2007). Physical model for the decay and preserva-
580 tion of marine organic carbon. *Science*, *316*(5829), 1325. doi: 10.1126/science
581 .1138211
- 582 Schwinger, J., Goris, N., Tjiputra, J. F., Kriest, I., Bentsen, M., Bethke, I.,
583 ... Heinze, C. (2016). Evaluation of noresm-oc (versions 1 and 1.2),
584 the ocean carbon-cycle stand-alone configuration of the norwegian earth
585 system model (noresm1). *Geosci. Model Dev.*, *9*(8), 2589–2622. doi:
586 10.5194/gmd-9-2589-2016
- 587 Suess, E. (1980). Particulate organic carbon flux in the oceans—surface productivity
588 and oxygen utilization. *Nature*, *288*(5788), 260–263. doi: 10.1038/288260a0
- 589 Vähätalo, A. V., Aarnos, H., & Mäntyniemi, S. (2010). Biodegradability con-
590 tinuum and biodegradation kinetics of natural organic matter described by
591 the beta distribution. *Biogeochemistry*, *100*(1), 227–240. doi: 10.1007/
592 s10533-010-9419-4
- 593 Volk, T., & Hoffert, M. I. (1985). Ocean carbon pumps: Analysis of relative
594 strengths and efficiencies in ocean-driven atmospheric CO₂ changes. In
595 T. E. Sundquist & W. S. Broecker (Eds.), *The carbon cycle and atmospheric*
596 *CO₂: Natural variations Archean to present*. (Vol. 32, pp. 99–110). American
597 Geophysical Union, Washington, D. C.
- 598 Wilson, J. D., Barker, S., Edwards, N. R., Holden, P. B., & Ridgwell, A. (2019).
599 Sensitivity of atmospheric CO₂ to regional variability in particulate organic
600 matter remineralization depths. *Biogeochemistry*, *16*(14), 2923–2936. doi:

601 10.5194/bg-16-2923-2019

602 Yamanaka, Y., & Tajika, E. (1996). The role of the vertical fluxes of particulate
603 organic matter and calcite in the oceanic carbon cycle: Studies using an ocean
604 biogeochemical general circulation model. *Global Biogeochem. Cycles*, 10(2),
605 361–382. doi: 10.1029/96GB00634

606 Yamanaka, Y., & Tajika, E. (1997). Role of dissolved organic matter in the marine
607 biogeochemical cycle: Studies using an ocean biogeochemical general circula-
608 tion model. *Global Biogeochem. Cycles*, 11(4), 599–612.